




RESEARCH ARTICLE | MARCH 04 2021

## Euler–Lagrange study of bubble breakup and coalescence in a turbulent boundary layer for bubble drag reduction

Xiaosong Zhang (张晓嵩); Jianhua Wang (王建华) ; Decheng Wan (万德成)  



*Physics of Fluids* 33, 037105 (2021)

<https://doi.org/10.1063/5.0037962>



## Physics of Fluids

Special Topic:

John Michael Dealy (1937-2024): Celebrating His Life

Guest Editors: Alan Jeffrey Giacomini and Savvas G. Hatzikiriakos

[Submit Today!](#)

# Euler-Lagrange study of bubble breakup and coalescence in a turbulent boundary layer for bubble drag reduction

Cite as: Phys. Fluids **33**, 037105 (2021); doi: [10.1063/5.0037962](https://doi.org/10.1063/5.0037962)

Submitted: 18 November 2020 · Accepted: 25 January 2021 ·

Published Online: 4 March 2021





View Online



Export Citation



CrossMark

Xiaosong Zhang (张晓嵩),<sup>1</sup> Jianhua Wang (王建华),<sup>1</sup>  and Decheng Wan (万德成)<sup>1,2,a)</sup> 

## AFFILIATIONS

<sup>1</sup>Computational Marine Hydrodynamics Lab (CMHL), School of Naval Architecture, Ocean and Civil Engineering, Shanghai Jiao Tong University, Shanghai 200240, China

<sup>2</sup>Ocean College, Zhejiang University, Zhoushan 316021, China

<sup>a)</sup>Author to whom correspondence should be addressed: [dcwan@sjtu.edu.cn](mailto:dcwan@sjtu.edu.cn). URL: <https://dcwan.sjtu.edu.cn/>

## ABSTRACT

By injecting bubbles on the surface of ships or underwater vehicles, friction resistance can be effectively reduced. This technique is known as bubble drag reduction (BDR). The Euler–Lagrange method has been proved to be an effective numerical method in the study of the BDR mechanism. Bubble diameters were uniform in previous Euler–Lagrange simulations. However, many experimental results indicated that there is a nonuniform bubble size distribution under the action of turbulence, which affects the drag reduction significantly. In this paper, the authors developed a Euler–Lagrange code with the ability to simulate bubble breakup and bubble coalescence. The process of BDR on a flat plate is simulated by injecting bubbles into a turbulent boundary layer flow. Diameters of the bubbles are the same when they are injected into the flow field. During the simulation, bubbles of varying sizes can be clearly simulated in the evolution process due to breakup and coalescence. The drag reduction effect and bubble size distribution are validated by comparison with previous experimental data. Numerical results with and without breakup and coalescence models are discussed in detail to illustrate the advantage of the present algorithm. Moreover, bubble size distribution, bubble trajectory, and bubble induced turbulent modulation are analyzed in detail to explain the mechanism and its relationship with bubble size distribution.

Published under license by AIP Publishing. <https://doi.org/10.1063/5.0037962>

## I. INTRODUCTION

Skin frictional resistance accounts for more than half of the total drag for low-speed ships with full hull, such as cargo ships and tankers.<sup>1</sup> Therefore, reducing skin frictional resistance is always an important goal in shipping research.<sup>2</sup> The bubble drag reduction (BDR) technique has been a focus in recent years, in which bubbles are injected into the bottom of the ship and cover the bottom surface to reduce frictional resistance.<sup>3</sup> Many ship experiments have proved the significant drag reduction effect at model scale<sup>4,5</sup> and full scale.<sup>6</sup> At the same time, the underlying mechanisms still need to be further explored. The actual BDR process under the ship bottom plate is usually simplified into a problem that injecting bubbles into a turbulent boundary layer to carry out a fundamental study.

The experiment of bubble injection under a flat plate is one of the most important research methods. Many reliable data and flow states are obtained from previous experimental studies. Hassan *et al.*<sup>7</sup> built a turbulent water channel at Reynolds number  $Re_h = 5128$ . The

maximum drag reduction effect reached 38.4%. Ortiz-Villafuerte and Hassan<sup>8</sup> adopted the particle image velocimetry (PIV) technique to measure the water flow modulation induced by bubble injection. The results indicated that the velocity fluctuation along the flow direction is strengthened, and the velocity fluctuation along the wall-normal direction is weakened. Murai *et al.*<sup>9–11</sup> also carried out bubble channel flow experiments. They found that the near wall Reynolds stress was reduced, which was an important reason for drag reduction. Besides the drag reduction effect and flow data, detailed bubble images near the plate surface were provided. The images showed that most bubbles remain spherical under the action of large surface tension. However, the bubble sizes are nonuniform, and bubbles with different diameters form a special size distribution near the wall surface. In order to meet the needs of practical applications, a series of high Reynolds number ( $2.1 \times 10^8$ ) experiments<sup>12–14</sup> were carried out in the USA Navy's Large Cavitation Channel. The detailed bubble size distribution (BSD) at several down-stream positions was measured. Under the high speed

conditions, bubbles were smaller than the original size due to the impact of turbulence. While under the low speed conditions, bubbles coalesced to form an air layer, and the max drag reduction effect could reach 80%. Hara *et al.*<sup>15</sup> performed a microbubble drag reduction experiment and provided bubble size distribution at different stream-wise positions by detailed image analysis. Their results are used to validate the numerical simulation in this paper. More recently, Paik *et al.*<sup>16</sup> carried out visualization investigation for bubble behaviors in the turbulent boundary layer. A microbubble generator was used to produce bubbles with diameters in the range 5–100  $\mu\text{m}$ . The results showed that bubbles with different diameters behaved differently in the turbulent boundary layer, which would affect the drag reduction effect.

It is still a difficult problem to fully measure and count the complex bubble flow data in the experiment. However, numerical simulation has the advantage of extracting the flow information and has been applied in BDR investigation. The two-fluid model (TFM) in the Euler framework is one of the most commonly used modeling methods, in which both the water phase and bubble phase are modeled by Navier–Stokes equations. This method can be used in simulations with a large amount of bubbles due to the low computational cost. Kunz *et al.*<sup>17</sup> employed an ensemble averaged multifield two-fluid baseline differential model to simulate the BDR problem at a high Reynolds number. The numerical results were compared with experimental data and were proved to be qualitatively correct. In order to overcome the accuracy shortcomings, Kunz *et al.*<sup>18</sup> improved their code and calculated the bubble breakup and coalescence by the interfacial area density transport (IADT) model. Detailed validation studies were performed across a wide range of Reynolds numbers. A similar model was adopted by Zhao *et al.*<sup>19</sup> to study the drag reduction effect with different bubble sizes. Expect the IADT model, more scholars adopted the population balance model (PBM) to simulate bubble breakup and coalescence in Euler two-fluid simulations. Mohanaragam *et al.*<sup>20</sup> adopted a population balance approach based on the multiple-size-group (MUSIG) model to account for the bubble size distribution. The validity of numerical models is verified by comparison with experimental data. Qin *et al.*<sup>21</sup> carried out both numerical simulation and the experimental test of BDR on a flat plate. Bubble size distributions at different air flow rates were predicted well, and streamwise characteristics of the drag reduction effect were discussed in their study.

Although the drag reduction effect can be predicted accurately by the two-fluid model, the description of bubble dynamics is still unclear. Therefore, in order to further investigate the underlying physical mechanism, the Euler–Lagrange method was adopted to resolve the detailed bubble behavior of bubbles in the BDR problem. In this method, Navier–Stokes equations are used to solve hydrodynamics, and the kinematic equation is used to solve bubble dynamics. Xu *et al.*<sup>22</sup> combined the direct numerical simulation (DNS) and Lagrange bubble tracking to simulate BDR in a channel flow. By means of the accurate numerical method, the modification of turbulent structures in the near-wall region was discussed in detail. Ferrante and Elghobashi<sup>23</sup> applied the same numerical method and studied the change of fluid velocity induced by bubble injection in a turbulent boundary layer. They found a local positive of the fluid velocity in the near wall region, which was regarded as a contribution to the drag reduction. Mattson and Mahesh<sup>24</sup> carried out a one-way

coupled Euler–Lagrange simulation and focused on the bubble migration in the turbulent boundary layer. The effect of different hydrodynamic forces on the behavior of bubbles was verified. The interaction of bubbles and liquid turbulence was the dominating topic of the previous two-way coupled Euler–Lagrange simulation. Vertical<sup>25,26</sup> and horizontal<sup>27</sup> channel flows laden with bubbles were the main research condition. The two-way coupling was achieved by interface models and the coupled source term in the momentum equation. The main conclusion agreed upon in these studies is that bubbles reduce Reynolds stress and turbulent kinetic energy in the near wall region, which is an important mechanism of drag reduction. The DNS method was adopted for the fluid solution of the above studies. The Reynolds number was relatively low, and the bubble diameter was uniform and small. Asiagbe *et al.*<sup>28</sup> adopted the large eddy simulation (LES) model to solve the liquid phase in Euler–Lagrange simulation. Their results proved that the velocity fluctuations and flow modification induced by bubbles could also be resolved by LES simulation with less computational cost. Zhang *et al.*<sup>29</sup> proposed a Gaussian distributed two-way coupled algorithm to overcome the numerical instability when the bubble diameter was larger than the grid size. Bubble collision was also considered in the BDR simulation, and bubble trajectory was discussed in detail. It is worth noting that bubble diameters were uniform in all the Euler–Lagrange studies described above, meaning that bubble breakup and coalescence were ignored.

Summing up the previous studies introduced above, it can be found that the lack of bubble breakup and coalescence simulation is an important flaw in the current Euler–Lagrange studies. In many experiments, it has been observed that the breakup and coalescence of bubbles will lead to the formation of nonuniform bubble size distribution, which has a great impact on the drag reduction effect. In the TFM numerical studies, the singleness of the bubble attribute is originally a disadvantage of the TFM model, but the bubble size distribution has been successfully predicted by the combination of the PBM model. It has been proved that better results can be obtained with accurate BSD prediction. The PBM model is a statistical method. In the Euler–Lagrange method, since each bubble is tracked individually, the simulation of bubble breakup and coalescence can be realized by means of more physical models. Unfortunately, these kinds of bubble behaviors have not been simulated in previous Euler–Lagrange studies. The main goal of the present study is to develop a Euler–Lagrange code for BDR simulation with the consideration of bubble breakup and coalescence. The critical Weber number model is used as the criterion of breakup. The contact and elastic collision between bubbles are fully solved, and the coalescence of bubbles is performed based on the contact time. The visualization results and statistical analysis of bubbles are presented.

## II. MATHEMATICAL MODELING

In the present Euler–Lagrange study, the liquid and bubble are treated as the continuous phase and the discrete phase, respectively. Each bubble is tracked by the kinematic equation following Newton's second law. The liquid phase is governed by Navier–Stokes equations. Two-way coupling is realized by hydrodynamic force models and coupled source term in the momentum equation. The mathematical models for different phase calculation and coupling are introduced in detail as follows.

### A. Liquid phase solving

It is important to simulate the liquid flow fluctuations to further study the bubble evolution. According to previous studies,<sup>28,29,51</sup> the LES model has been proved to be an effective method to solve the flow fluctuations in turbulent boundary layer flow. Therefore, it is used for the simulation of the liquid phase. A box filter is adopted to filter the eddy in the flow field. The large-scale eddy is directly solved, while the small-scale eddy is approximated by the sub-grid model. The filtered continuity and momentum equations are written as

$$\frac{\partial \alpha}{\partial t} + \frac{\partial \alpha \bar{u}_i}{\partial x_i} = 0, \quad (1)$$

$$\frac{\partial \alpha \bar{u}_i}{\partial t} + \bar{u}_j \frac{\partial \alpha \bar{u}_i}{\partial x_j} = -\frac{1}{\rho} \frac{\partial \bar{p}}{\partial x_i} - \frac{\partial}{\partial x_j} (\bar{\sigma}_{ij} + \tau_{ij}) + \alpha g + \frac{f_{pf}}{\rho_l}, \quad (2)$$

where the overbar identifies filtered quantities.  $u_i$  is the fluid velocity in three directions ( $i = x, y, z$ ),  $\alpha$  is the liquid phase volume fraction,  $\rho_l$  is the liquid density,  $p$  is the pressure,  $\sigma_{ij}$  is the viscous stress, and  $f_{pf}$  is the coupled source term, which reflects the effect of bubbles on the liquid. The subgrid scale (SGS) stress tensor  $\tau_{ij}$  is given by

$$\tau_{ij} = \bar{u}_i \bar{u}_j - \bar{u}_i \bar{u}_j. \quad (3)$$

The wall adapting local eddy-viscosity model (WALE)<sup>30</sup> is used to model the SGS stress. The turbulent kinematic eddy viscosity is defined as

$$\nu_t = (C_w \Delta)^2 \frac{(S_{ij}^d S_{ij}^d)^{3/2}}{(\bar{S}_{ij} \bar{S}_{ij})^{5/2} + (S_{ij}^d S_{ij}^d)^{5/4}}, \quad (4)$$

where the filter width  $\Delta$  is calculated by  $\Delta = V^{1/3}$ .  $C_w$  is a constant model coefficient. Simulation by the model proposer has shown that  $C_w$  equals 0.5, which is appropriate for the homogenous isotropic turbulence (HIT). Since most of the practical flow problems, including the turbulent boundary layer flow studied in this paper, are inhomogeneous and highly anisotropic,  $C_w$  should be decreased to model the flow characteristics. At present,  $C_w = 0.325$  is widely accepted,<sup>31</sup> which is also used in this work.  $S_{ij}$  is the strain-rate tensor, which satisfies

$$S_{ij}^d = \frac{1}{2} (\bar{g}_{ij}^2 + \bar{g}_{ji}^2) - \frac{1}{3} \delta_{ij} \bar{g}_{kk}^2, \quad \bar{g}_{ij} = \frac{\partial \bar{u}_i}{\partial x_j}. \quad (5)$$

### B. Bubble dynamics tracking

Bubbles are assumed to be nondeformable spheres under the action of large surface tension. The motion of bubbles can be solved by the kinematic equation constructed by various hydrodynamic forces. The governing equation is written as

$$\begin{aligned} m \frac{dv}{dt} &= f_D + f_L + f_P + f_G + f_C \\ &= \frac{3mC_D}{4d} |u - v| (u - v) + \frac{m\rho_l}{\rho_b} C_L (u - v) \times (\nabla \times u) \\ &\quad + \frac{m\rho_l}{\rho_b} \frac{Du}{Dt} + mg \left( 1 - \frac{\rho_l}{\rho_b} \right) + f_C, \end{aligned} \quad (6)$$

where  $v$  is the bubble velocity,  $m$  is the mass of bubble,  $d$  is the bubble diameter, and  $\rho_l$  and  $\rho_b$  represent the liquid density and bubble

density, respectively. The terms on the right side of Eq. (6) represent the drag force, shear lift force, fluid acceleration force, gravity buoyancy, and collision force, respectively. The drag force coefficient ( $C_D$ ) and lift force coefficient ( $C_L$ ) are determined by Tomiyama's drag model<sup>32</sup> and the lift model<sup>33</sup> as follows:

$$C_D = \max \left( \min \left( \frac{16}{Re(1 + 0.15Re^{0.687})} \frac{8}{3} \frac{Eo}{Eo + 4}, \frac{8}{3} \frac{Eo}{Eo + 4} \right), \frac{8}{3} \frac{Eo}{Eo + 4} \right), \quad (7)$$

$$C_L = \begin{cases} \min[0.288 \tan h(0.121Re), f(Eo_d)], & Eo_d < 4, \\ f(Eo_d), & 4 < Eo_d < 10.7, \end{cases}$$

$$f(Eo_d) = 0.00105Eo_d^3 - 0.0159Eo_d^2 - 0.0204Eo_d + 0.474, \quad (8)$$

where the bubble Reynolds number is defined as  $Re = \frac{d|u-v|}{\nu}$  and the Eötvös number ( $Eo$ ) is defined as  $Eo = \frac{g\rho_l - \rho_b}{\sigma} d^2$ , where  $\sigma$  is the surface tension coefficient, which is 0.072 N/m in the present study.  $Eo_d$  is defined as  $\frac{g\rho_l - \rho_b}{\sigma} d_H^2$ , where  $d_H = d(1 + 0.163Eo^{0.757})$ . The selection of drag and lift models mainly affects the velocity of bubbles, thus affecting the spatial distribution. A larger drag coefficient makes the bubble velocity more likely to be the same as the surrounding liquid flow, while a larger lift coefficient causes the bubbles to move more obviously in the direction perpendicular to the main flow. The models adopted in the present work are derived from experiment tests of Tomiyama *et al.*<sup>32,33</sup> and the effectiveness has been validated in our previous study.<sup>29</sup>

The collision force  $f_c$  is calculated by the sum of an elastic force and a viscous force. A nonlinear collision force model proposed by Heitkam *et al.*<sup>34</sup> is adopted in this paper to describe the bubble–bubble interaction and bubble–wall interaction. The elastic and viscous contact forces can be written as

$$F_{elastic} = 18.5\sigma \left( \frac{\Delta}{R_{eq}} \right)^2 + 2.0\Delta\sigma, \quad (9)$$

$$\begin{aligned} F_{viscous} &= uC_{bc} \frac{12\mu_l}{2\pi} 0.34 \left( \frac{\Delta}{R_{eq}} + 0.0002 \right)^{-0.5} \\ &\quad \times \left( 4.0 \sqrt{\frac{R_{eq}^3}{h_0}} + 3.0R_a \frac{R_{eq}}{h_0} \right), \end{aligned} \quad (10)$$

where  $R_{eq}$  is the effective radius,  $\Delta$  is the deformation of the bubble, and  $h_0$  is the gap width when the bubble approaches another bubble or a wall. The parameter  $C_{bc}$  represents the collision partner, which is equal to 1 for bubble–wall collision and 0.25 for bubble–bubble collision. In fact, bubble–bubble collision has little influence on this problem. However, the bubble–wall collision will affect the relative position of the bubble and the wall surface, resulting in the change of the local void fraction. A “harder” collision model with a large coefficient in Eq. (9) may lead to the consequence that the bubbles are difficult to adhere to the plate, resulting in a reduction in the void fraction. The applicability of this model in bubble–wall interaction and BDR simulation has been validated in previous work.<sup>29</sup>

### C. Two-phase coupling

It is obvious that the bubble motion is controlled by the hydrodynamic force as Eq. (6), which is called one-way coupling. A two-way

coupled algorithm means that the effect of bubbles on the liquid can also be modeled.<sup>35</sup> The coupled effect includes two parts. First, in terms of mass conservation, the volume of bubbles in the flow field should be removed, which forms the volume fraction. Second, in terms of momentum conservation, bubble motion leads to coupled forces acting on the liquid flow. The coupled forces can be calculated as the reaction force of the hydrodynamic forces on bubbles.

Because both phases are defined in different frameworks (i.e., Lagrange and Euler), the most important problem is to employ a reasonable mapping technique to achieve two-way coupling. A Gaussian bubble volume distribution scheme is adopted to overcome the numerical instability when the bubble is larger than grid size. For example, the void fraction in a cell  $i$  can be calculated using

$$\alpha_i = \frac{\sum_{j=1}^{N_i} f_{k,j} V_j^b}{\sum_{k=1}^{N_{cells}} (V_k^{cell} f_{k,j})}; \quad f_{k,j} = \frac{1}{(\sqrt{2\pi}S)^3} e^{-\left(\frac{|x_{kj}|^2}{2S^2}\right)}, \quad (11)$$

where  $N_i$  is the number of bubbles in the affected region of cell  $i$ ,  $V_j^b$  is the volume of bubble  $j$ ,  $N_{cells}$  is the number of cells in the affected region of bubble  $j$ ,  $V_k^{cell}$  is the volume of cell  $k$ ,  $f_{k,j}$  is the Gaussian weight function adopted in the present study,  $|x_{kj}|$  represents the distance between cell  $k$  and bubble  $j$ , and  $S$  is the standard deviation. Both the volume fraction and coupled forces are smoothed by this scheme. A detailed derivation of Eq. (11) is described in our previous study.<sup>29</sup>

## D. Bubble breakup

The numerical simulation of bubble breakup consists of two key parts. One is the breakup critical criterion, and the other is the daughter bubble size distribution.

The critical criterion of bubble breakup is directly related to the physical phenomena. The physical breakup mechanisms can be classified into four main categories: turbulent fluctuation and collision, viscous shear stress, shearing off process, and interfacial instability.<sup>36,46</sup> Among these mechanism problems, bubble breakup due to turbulent fluctuation and collision has been most extensively studied.<sup>36</sup> At the same time, this mechanism has been regarded as the dominant breakup mechanism for bubble moving in turbulence flow like the BDR process. In this kind of physical problem, the most important physical quantities are turbulent kinetic energy and bubble surface energy. Turbulent kinetic energy represents the perturbation of surrounding liquid flow, while bubble surface energy represents the ability to keep its original shape. By dimensionless analysis, the breakup critical criterion can be written in terms of a Weber number as follows:

$$We = \frac{\rho_l \overline{\delta u^2(d)} d}{\sigma}, \quad (12)$$

where  $\rho_l$  is the liquid density,  $d$  is the bubble diameter,  $\sigma$  is the surface tension coefficient, and  $\overline{\delta u^2(d)}$  is the mean square liquid velocity difference over the bubble diameter.

Based on the Weber number, many literature studies proposed using a constant critical value  $We_{crit}$  to be the criterion. One of the most popular models proposed by Prince and Blanch<sup>37</sup> is  $We_{crit} = 2.3$  for air bubbles in water. Risso and Fabre<sup>38</sup> carried out experiments under microgravity conditions and analyzed single bubble breakup in the turbulent jet. Finally, they suggested that the critical Weber

number approximates to 2.7–2.8. Kolev<sup>39</sup> indicated that for turbulence acceleration induced bubble breakup, the most frequently used value for the hydrodynamic stability in the two-phase literature is  $We_{crit} \approx 12$ . Obviously, it is hard to find a constant critical Weber number value that is suitable for all conditions. Therefore, some scholars proposed a critical Weber number model related to bubble characteristics.<sup>40,41</sup> Recently, Lau *et al.*<sup>36</sup> established a critical Weber number model for the Euler–Lagrange framework, which is adopted in this paper. The criterion is defined as

$$We = \frac{\rho_l \overline{\delta u^2(d)} d}{\sigma} > We_{crit} = 12 \cdot \zeta; \quad \zeta = \left( \frac{1 + 2E_b^p}{3E_b^{2/3p}} \right)^{-1/p}, \quad (13)$$

where  $p = 1.6075$ , and  $E_b = f(Eo_d)$  is been shown in Eq. (8). This model is derived from the analysis of bubble deformation in turbulence flow.

As most breakup models in the literature, bubble breakup is assumed to be binary in the present study. Sizes of the daughter bubbles after breakup conform to a specific statistical distribution. Based on previous theoretical analysis and experimental measurements, it can be summarized that there are mainly four types of distributions: uniform distribution,<sup>37,42</sup> bell-shape distribution,<sup>37</sup> U-shape distribution,<sup>40</sup> and M-shape distribution.<sup>43</sup> Among these distribution models, Nambiar *et al.*<sup>44</sup> pointed out that the U-shape distribution model has the strongest physical foundation. It stands for the mechanism that equal size binary breakup consumes the most energy, resulting in the lowest probability of occurrence. Therefore, the U-shape model is adopted in the present work. The probability density function can be written as

$$f_{bv}(\gamma) = \frac{\Gamma(1)}{\Gamma(0.5)\Gamma(0.5)} \gamma^{-\frac{1}{2}} (1-\gamma)^{-\frac{1}{2}}, \quad (14)$$

where  $\Gamma$  is the gamma function and  $\gamma$  is a random value between 0 and 1.

For the numerical implementation, each individual bubble is evaluated by the breakup criterion (13) before solving the kinematic equation (6). The evaluation is performed at every time step; therefore, the corresponding breakup frequency is  $f_{Breakup} = \frac{1}{\Delta t}$ . If the criterion is satisfied, the bubble breaks into two daughter bubbles whose diameter is determined by the distribution model (13). The larger daughter bubble is located at the original position of the parent bubble, while the smaller daughter bubble is located at a random position near the original position. As Fig. 1 shows,  $r$  is a random vector whose magnitude equals  $0.6 \times (d_A + d_B)$ . A coefficient of 0.6 is determined by a combination of numerical and physical considerations. A value less than 0.5 will cause the two daughter bubbles to overlap, resulting in numerical

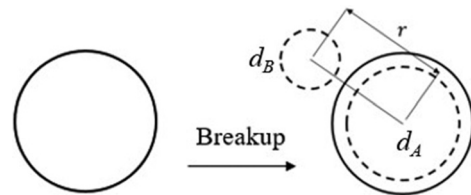


FIG. 1. Illustration of the numerical model of bubble breakup.



oscillation. A too large value will cause the two daughter bubbles to be too far apart, which does not correspond to physical phenomena. Therefore, 0.6 is recommended in the present algorithm.

The selection of the breakup criterion and daughter bubble size distribution function will affect the calculated bubble size. For the criterion, the lower the threshold of the breakup criterion, the easier the breakup of bubbles, resulting in smaller bubble sizes. For the distribution function, the Bell-shape distribution will produce more equal-size breakup, while the U-shape distribution tends to produce daughter bubbles of obviously different sizes. Actually, there is no universal model suitable for all kinds of complex flows at present. Some quantitative comparisons were carried out in our previous studies<sup>45</sup> and can lay a foundation for the application of this work.

In order to guarantee the numerical stability, a loop process is implemented to find a fine position that there is no overlap between the new daughter bubbles and the surrounding bubbles. After the positions of two daughter bubbles are determined, the velocities are set to be equal to the parent bubble velocity. The whole algorithm of bubble breakup is summarized as shown in Fig. 2.

### E. Bubble coalescence

Many kinds of models have been proposed to describe the process of bubble coalescence. The film drainage model<sup>37</sup> is one of the most widely accepted bubble coalescence models and has been adopted in the present study. The bubble coalescence process is divided into three stages in the film drainage model. First, bubbles are close to each other, and there is a thin liquid film between them. Second, as bubbles are further closer, the film gradually drains and thins. Finally, the liquid film drains out to a critical thickness and coalescence occurs. The criterion is that the duration of contact bubbles must be longer than a critical time called “drainage time.” The drainage time is defined as

$$t_{\text{drainage}} = \sqrt{\frac{d_{eq}^3 \rho_l}{128\sigma}} \ln \left( \frac{\theta_0}{\theta_f} \right), \quad (15)$$

where  $\theta_0$  and  $\theta_f$  are the initial liquid film thickness and final liquid film thickness, respectively.  $\theta_0$  is set to be  $10^{-4}$  and  $\theta_f$  is set to be  $10^{-8}$  for the air-water system, which are recommended by previous numerical<sup>46</sup> and experimental<sup>47</sup> studies. If the ratio of  $\theta_0$  to  $\theta_f$  is increased, the frequency of bubble coalescence will decrease, which may lead to smaller size distribution of the calculated bubble cloud. The equivalent radius  $d_{eq}$  is defined as

$$d_{eq} = 2 \left( \frac{1}{d_A} + \frac{1}{d_B} \right)^{-1}. \quad (16)$$

In many previous Euler-Lagrange studies using hard spheres to calculate bubble collision, additional models are still needed to calculate the contact time because the collision is assumed to be instantaneous. However, this approximation can be eliminated in the present simulation because the contact and elastic collision are solved.

For the numerical implementation, bubble coalescence and collision have the same priority in the solution. The bubble interaction pair list is established and updated in every time step. A variable  $t_{\text{contact}}$  is used to record the cumulative contact time for each bubble pair. Bubble pairs are evaluated by the coalescence criterion (15). If the criterion is satisfied, the bubble-bubble interaction is solved as coalescence, otherwise as collision. The two bubbles that coalesce are removed, and a new bubble is created as Fig. 3 shows.

The diameter and velocity of the new bubble are updated to keep mass and momentum conservation. The expressions are shown as follows:

$$d_C = (d_A^3 + d_B^3)^{1/3}, \quad U_C = \frac{d_A^3 U_A + d_B^3 U_B}{d_A^3 + d_B^3}. \quad (17)$$

The whole algorithm of bubble coalescence is summarized as shown in Fig. 4.

The algorithm implementation and equation solution are performed using a self-developed solver based on the open source code OpenFOAM. To summarize the above introduction of numerical methods, the simulation of bubbly flow physical phenomena in the current solver includes the motion of microbubbles under the action of liquid flow, the bubble volume decrease caused by breakup, and the bubble volume increase caused by coalescence. At the same time, there are some physics about bubbly flow, which are not included in the present solver. First, the deformation of the bubble surface, including shape changes during breakup and coalescence, is not considered. In the problems simulated in this study, most of the bubbles are microbubbles less than  $200 \mu\text{m}$ , which are difficult to produce obvious deformation in practice and have a very short coalescence and breakup time. Therefore, the assumption of this method is reasonable.

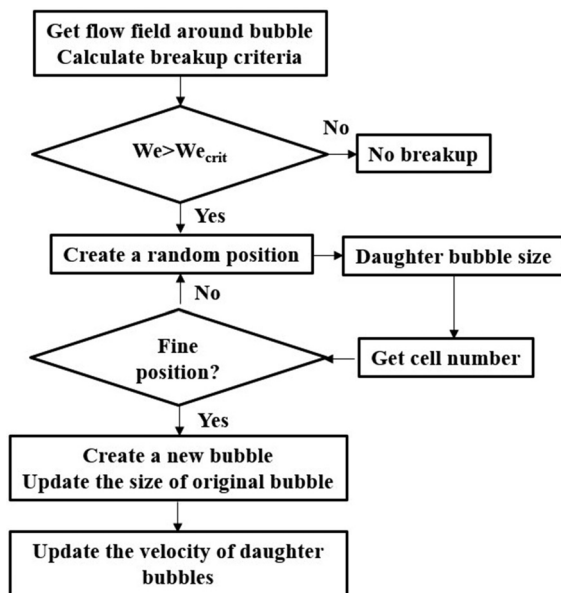


FIG. 2. Flowchart of the bubble breakup algorithm.



FIG. 3. Illustration of the numerical model of bubble coalescence.

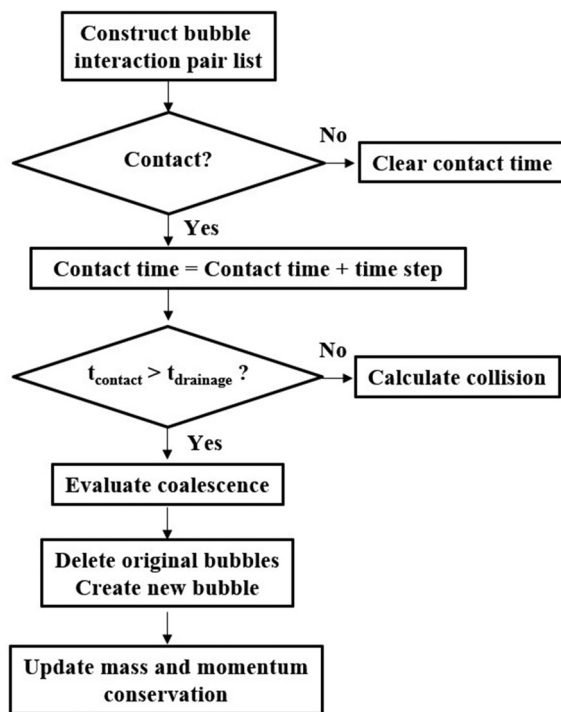


FIG. 4. Flowchart of the bubble coalescence algorithm.

However, this assumption causes errors for problems with bubble sizes in centimeters or several millimeters, and the method cannot be used for the problems of bubble volume change, such as cavitation. Second, continuous phase interface cannot be solved, which indicates that the physical phenomena of air water stratification cannot be simulated. For the combined implementation and computational stability of the above algorithms, careful design is carried out in this study. However, it can also be seen that the simulation method contains many models, which is also an inevitable problem for simulation based on the Euler–Lagrange method. Therefore, while introducing the models, we have tried to clarify the source of parameter selection and its possible influence on the calculation results. It is recommended to perform necessary attempts on model parameters when simulating different complex problems.

### III. COMPUTATIONAL CONDITIONS

A box domain is set to create a wall-bound turbulent boundary layer. Illustration of the computational domain and boundary conditions is shown in Fig. 5. The top wall is set to be a no-slip boundary to simulate turbulent flow under a plate. Bubbles are injected into the flow field at the front end of the plate. The lower, front, and back boundaries are set to be a symmetry plane. The inflow boundary is divided into two parts, uniform inflow and turbulent inflow. The boundary condition of the main flow region away from the plate is uniform inflow with constant velocity, while the boundary condition of the boundary layer region near the plate is turbulent inflow obtained from precursor turbulent flow simulation.

Numerical simulation parameters are chosen from the experiments of Hara *et al.*<sup>15</sup> They carried out a microbubble drag reduction

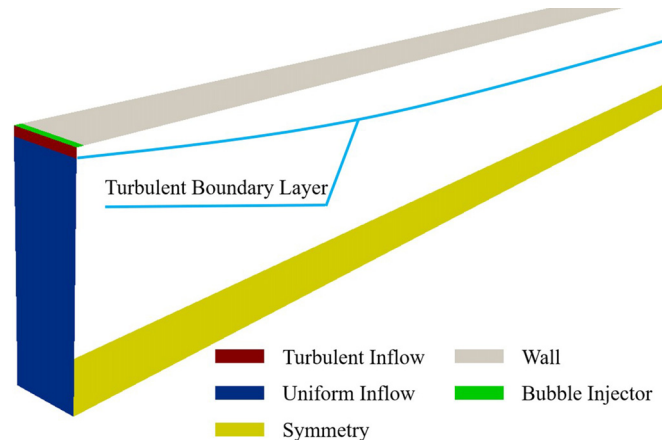


FIG. 5. Illustration of the computational domain.

test in a horizontal water channel. Detailed bubble size distribution and turbulent flow modulation were provided, benefiting from the arrangement of the optical system and particle tracking velocimetry. The results can be used to validate the present numerical solver. The air injector was placed at 625 mm from the test section entrance, and the measurement points were arranged within 1000 mm of the injector. Flow velocity  $U_0$  was 1.1 m/s based on the PIV test. Using a power law to estimate boundary-layer momentum thickness, the corresponding Reynolds number of the turbulent boundary layer is  $1553 < Re_\theta < 3337$ . In order to concentrate the spatial resolution to solve the streamwise and wall-normal direction flow details, the computation domain is set to cover the whole length and 1/4 width of the channel in the experiment. The height of the computational domain is set to ensure that the boundary layer never occupies more than one-third of the domain. Specifically, the length is  $L = 1100$  mm, the width is  $W = 25$  mm, and the height is  $H = 100$  mm. BDR with three different air flow rates is simulated:  $Q = 30.25$  mm<sup>3</sup>/s,  $Q = 60.5$  mm<sup>3</sup>/s, and  $Q = 90.75$  mm<sup>3</sup>/s, respectively. Air was injected from an electrode array in the experiment. In the simulations, bubbles are injected from a boundary with the same area of the electrode array. The initial bubble diameter is set to be 200  $\mu$ m as the experimental measurement. Computational parameters are summarized in Table I.

Precursor channel flow simulation proposed by Mukha and Liefvendahl<sup>48</sup> is adopted in the present study to generate specified turbulent boundary layer inflow data. A fully developed turbulent

TABLE I. Computational parameters.

Parameter	Specific value
Domain size $L \times W \times H$	1100 mm $\times$ 25 mm $\times$ 100 mm
Height of turbulent inflow $\delta$	18 mm
Liquid flow velocity $U_0$	1.1 m/s
Air flow rate $Q$	30.25, 60.5, 90.75 mm <sup>3</sup> /s
Initial bubble diameter	200 $\mu$ m
Density $\rho_l/\rho_b$	1000/1.2 kg/m <sup>3</sup>
Kinematic viscosity $\nu_l/\nu_b$	$1 \times 10^{-6}/1.48 \times 10^{-5}$

channel flow simulation is carried out first, in which the main parameters including the channel height ( $\delta = 18$  mm) and bulk velocity ( $U_b = 0.97$  m/s) are calculated by the momentum thickness and velocity of the target turbulent boundary layer. The channel flow simulation is initialized by a uniform flow field, and the development of the turbulent structure can be directly reflected from the monitoring of wall shear stress. At first, flow in the channel is laminar, and the shear stress decreases with time. After the transition, the shear stress increases rapidly and then oscillates around a fixed value. The flow field presents turbulent characteristics and reaches statistically a steady state. This process requires a simulation time of  $t^+ > 1800 \delta/U_b$ . Then, flow data are sampled from a slice in the domain at every time step. The sampled data are converted into an appropriate input format for the turbulent boundary layer simulation by a python package *eddylicious*.<sup>49</sup> The turbulent boundary layer flow simulation is initialized from zero velocity and no bubble injection. The simulation runs for time  $t_1^+ > 2L/U_0$  to guarantee that the turbulent boundary layer develops throughout the domain. Then, bubbles are injected into the flow field according to specified air flow rates. The simulation further runs for time  $t_2^+ > 3L/U_0$  to ensure the calculated physical quantities to achieve convergence. Finally, the results are extracted for analysis.

Adequate spatial resolution is a key factor to solve the flow in the turbulent boundary layer successfully. Grids in the streamwise and spanwise directions are uniformly distributed, while grids in the wall-normal direction are proportionally distributed. Grid sizes in the present work refer to the recommendation of Georgiadis *et al.*<sup>50</sup> Necessary attempts have been made before the final grid distribution is decided. First, an initial grid height of the first layer to the wall surface is set hypothetically, and the grid sizes in the streamwise and spanwise directions are set according to the recommended proportion in the literature.<sup>50</sup> After calculation, grid distribution in the wall-normal direction is further modified until the calculated wall shear stress achieves convergence. The plate surface  $y^+$  should be approximately 1. On the basis, the grids in the streamwise and spanwise directions are properly modified and refined according to the comparison between the calculated results and standard DNS data. After several iterations, an adequate grid distribution is finally decided. The computational domain is discretized using  $N_x \times N_y \times N_z = 600 \times 100 \times 60$  structured grid points. In order to show the independency of the present grid distribution, a comparison with a finer grid distribution is performed, in which each grid is reduced by  $\sqrt{2}$  times in three dimensions and the total number of grids has increased by  $2\sqrt{2}$  times. The physical quantity wall shear stress is chosen for comparison because most of the flow characteristics are directly related to this crucial parameter. At the position  $Re_\theta = 1600$ , the calculated nondimensional  $2\tau_w/\rho U_0^2$  using the current grids and the refined grids is 0.00375 and 0.00384, respectively. Similar results show the rationality of the current grid distribution.

Before injecting bubbles, it is essential to validate the accuracy of turbulent flow simulation. Three important flow quantities are compared with standard data, including the mean streamwise velocity profile, Reynolds-stress profile, and wall shear stress distribution. Figure 6 shows the comparison of mean streamwise velocity profiles. For the comparison between LES results and experimental results,<sup>15</sup> velocity profiles at two streamwise measure points,  $x = 0.25$  m and  $x = 1$  m, are plotted. Limited by the testing capacity of the equipment, the experimental results in the near-wall region ( $y^+ < 30$ ) are not valid, but the

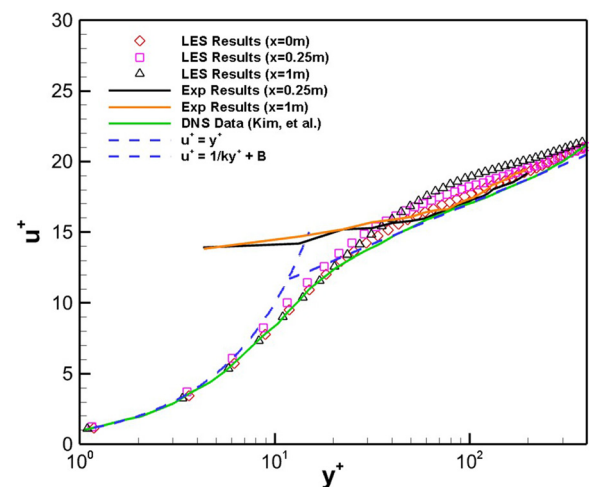


**FIG. 6.** Comparison of single-phase mean streamwise velocity profiles: present LES at  $x = 0$  m (rhombi), present LES at  $x = 0.25$  m (square), present LES at  $x = 0.25$  m (delta), experiment at  $x = 0.25$  m (black solid line), experiment at  $x = 0.25$  m (orange solid line), DNS data by Kim *et al.* (green solid line), and log-law with  $1/k = 2.5$  and  $B = 5.5$  (blue dashed line).

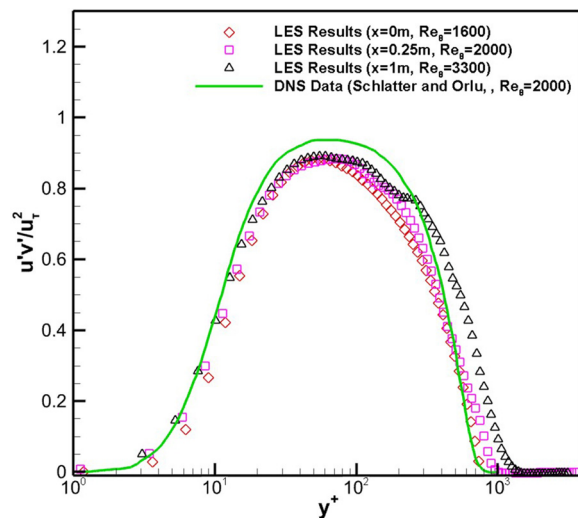
numerical results are in good agreement with the experimental results in the log-law region. In addition, the DNS results provided by Kim *et al.*<sup>51</sup> are also plotted. They carried out a turbulent channel flow simulation at Reynolds number  $Re_\tau = \frac{u_\tau h}{\nu} = 180$ , which is close to the inflow condition ( $Re_\tau = 270$ ) of the experimental test and the present LES simulation. In the experimental study paper<sup>15</sup> referred to in this paper, Hara *et al.* compared their velocity profile results with the DNS results of Kim *et al.* Therefore, their data are also used as standard data for comparison. Table II shows the quantitative error between the LES results and the DNS results. The error value is obtained by calculating the error of each data point on the velocity profile and taking the average value. It can be found that the flow calculation near the front is more accurate with an error of less than 5%. At the end of the computational domain ( $x = 1$  m), the error is 6.4%. The main source for the increased error is the slight overprediction of the velocity profile in the log-law region. The downstream error increases partly because the flow conditions at this location are different from those of DNS data. Referring to published papers<sup>48,49</sup> using the same LES model combined with the precursor channel flow method to simulate the turbulent boundary layer, the error of the velocity profile in the vicinity of 5% is acceptable. The result accords with the characteristics of the turbulent boundary layer velocity profile.

Figure 7 shows the comparison of Reynolds stress profiles. For the turbulent boundary layer simulated in the present study, the Reynolds numbers corresponding to  $x = 0$  m,  $x = 0.25$  m, and  $x = 1$  m are  $Re_\theta = 1600$ ,  $Re_\theta = 2000$ , and  $Re_\theta = 3300$ . Schlatter and Orlu<sup>52</sup> carried out DNS simulation for turbulent boundary layer flow and

**TABLE II.** Error of the velocity profile between LES results and DNS results.

Positions (m)	$x = 0$	$x = 0.25$	$x = 1$
Error (%)	2.6	4.9	6.4





**FIG. 7.** Comparison of single-phase Reynolds-stress profiles: present LES at  $x = 0$ ,  $Re_\theta = 1600$  (rhombi); present LES at  $x = 0.25$  m,  $Re_\theta = 2000$  (square); present LES at  $x = 1$  m,  $Re_\theta = 3300$  (delta); and DNS data by Schlatter and Orlu<sup>52</sup> at  $Re_\theta = 2000$  (green solid line).

provided Reynolds stress results at  $Re_\theta = 2000$ . Therefore, their data are plotted for comparison with the present results at the same Reynolds number. The quantitative comparison of Reynolds stress profiles is mainly about the location and magnitude of the stress peak. In the present work, the peak of the Reynolds stress occurs at  $y^+ = 74.9$ , and the nondimensional magnitude value is 0.883. However, in the DNS results, the peak of the Reynolds stress occurs at  $y^+ \approx 70$ , and the nondimensional magnitude value is 0.93. The calculated error is 7.0% and 5.0% for the peak location and magnitude, respectively. The Reynolds stress presents the characteristic of velocity fluctuations, which is more difficult to capture than the first order quantities. Referring to published papers<sup>51,52</sup> using the same LES model combined with the precursor channel flow method to simulate the turbulent boundary layer, the Reynolds stress error of less than 10% is acceptable. For the results at different streamwise directions, the profile of the Reynolds stress becomes wider gradually as the boundary layer thickens downstream, which is also consistent with the characteristics of turbulent boundary layers.

Finally, as a key parameter in the study of the drag reduction problem, the wall shear stress distribution along the flow direction is validated by DNS data<sup>52</sup> and empirical power law<sup>53</sup>  $C_f = 0.024Re_\theta^{0.25}$  as Fig. 8 shows. The results at four typical positions downstream are presented to represent the distribution of shear stress on the plate, corresponding to Reynolds numbers of  $Re_\theta = 1600$ , 2000, 2500, and 3000, respectively. The quantitative error between the present LES simulation and the empirical power law is shown in Table III. The error of the most accurate point is about 1%, while the largest error is 6.7%. According to the review of Schlatter and Orlu,<sup>52</sup> the error between the most previous published DNS simulation results and power law is about 1%–7% at similar Reynolds numbers. Therefore, the present LES simulation can be regarded as acceptable.

Simulations are performed on the high performance computing (HPC) cluster in the Computational Marine Hydrodynamics Lab,

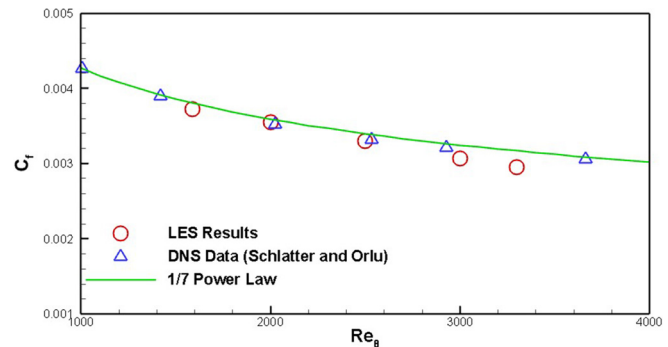


**FIG. 8.** Comparison of single-phase wall shear stress distributions: present LES results at typical positions (Circles), DNS data by Schlatter and Orlu (delta),<sup>52</sup> and low-Re 1/7 power law proposed by Smits *et al.* (green solid line).<sup>53</sup>

Shanghai Jiao Tong University. Each node consists of two central processing units (CPUs) with 18 cores per node and 64 GB accessible memory (Intel Xeon Gold 6240 at 2.6 GHz). 36 processors are assigned to calculate a case in parallel. The residual error tolerance of  $10^{-6}$  is used to ensure the convergence of the physical quantity solution at each time step. The monitoring of time history of typical physical quantities ensures the convergence of the calculated results. It costs approximately 30 h of clock time to complete a BDR simulation for  $Q = 30.25 \text{ mm}^3/\text{s}$  without modeling breakup and coalescence and 70 h with the modeling of breakup and coalescence. It is worth noting that the computational cost is obviously dependent on the number of bubbles. The significant increase in computing time is not mainly due to the new algorithms but due to the fact that the number of bubbles in the flow field has increased several times compared with the original case after considering breakup. At the same time, the computational time also increases with the increase in the air flow rate obviously. It costs approximately 150 h of clock time to complete a simulation for  $Q = 60.5 \text{ mm}^3/\text{s}$  and 230 h for  $Q = 90.75 \text{ mm}^3/\text{s}$ .

#### IV. RESULTS AND DISCUSSION

In this section, bubbles are injected into the turbulent boundary layer, which is generated in advance. By using the Euler–Lagrange solver with bubble breakup and coalescence modules, bubble behavior characteristics are discussed in detail. Then, the effects of bubbles on the water flow field are investigated, including drag reduction and turbulent modulation. Comparisons are carried out to illustrate the advantage of the present method in contrast with the previous one without bubble breakup and coalescence.

##### A. Bubble behavior characteristics

Simulation results with air flow rate  $Q = 30.25 \text{ mm}^3/\text{s}$  are taken as an example to analyze the bubble behavior characteristics. Both the overall view and local view of the bubble flow field can be seen in

**TABLE III.** Error of the wall shear stress between LES results and DNS results.

$Re_\theta$	1600	2000	2500	3000	3300
Error (%)	1.2	1.1	2.8	5.5	6.7

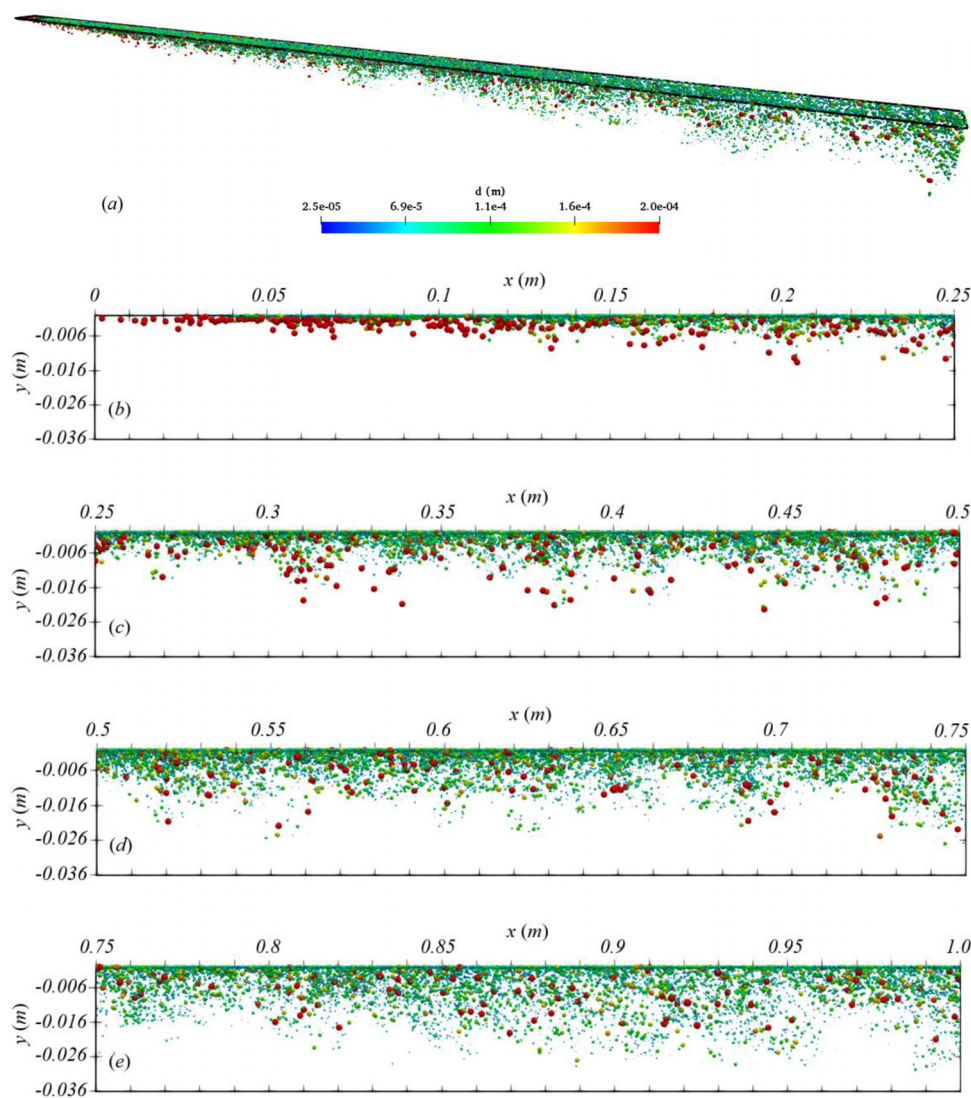


**FIG. 9.** Numerical simulation results of spatial bubble distribution with air flow rate  $Q = 30.25 \text{ mm}^3/\text{s}$ . The shown bubble size is 10 times the actual size. (a) Overall view of the whole flow field. (b)–(e) Local view within a specific streamwise position:  $x \in (0, 0.25)$ ,  $x \in (0.25, 0.5)$ ,  $x \in (0.5, 0.75)$ , and  $x \in (0.75, 1)$ .

**Fig. 9.** Bubbles are presented as spheres with different diameters. For a better view, the bubble size shown in the figure is 10 times the actual size. For the motion of the bubbles, it is obvious that a large number of bubbles migrate away from the upper wall downstream. A visual manifestation of this is that the bubbles are located farther and farther away from the plate. The bubble distribution shown in **Fig. 9** achieves a statistically steady state. In fact, each bubble has variation in its vertical position due to turbulent fluctuation in the present unsteady simulation. The maximum distance between the bubbles and the plate in four different downstream position intervals was extracted. The mean value  $D_{mean}$  and the root mean square (RMS) of the pulsation value  $D'_{RMS}$  are calculated over a period of time  $1L/U_0$ . The results are shown in **Table IV**. The average value can reflect the downstream characteristics of bubble movement, while the RMS value can reflect

the unsteady variation of bubble distribution. According to previous studies,<sup>24,29</sup> the migration is proved to be dominated by the fluid acceleration force of the turbulent flow. However, bubble size characteristics were not investigated in the previous numerical studies because of the lack of bubble breakup and coalescence modules in their code. It

**TABLE IV.** Maximum distance between the bubbles and the plate in four different downstream position ranges.

x ranges	(0, 0.25)	(0.25, 0.5)	(0.5, 0.75)	(0.75, 1)
$D_{mean}$ (m)	0.016 35	0.024 93	0.028 67	0.033 00
$D'_{RMS}$ (m)	0.002 21	0.001 31	0.001 10	0.001 66

can be seen from Fig. 9(b) that bubbles with a constant initial diameter are injected into the flow field. As the bubbles move downstream, obvious oscillation induced by the turbulence fluctuation appears during the bubble movement. At the same time, strong viscous shear and flow fluctuation produce a significant velocity difference around the bubbles, leading to the obvious breakup from initial bubbles to smaller bubbles. In the length range close to the injector, the bubbles are relatively close to the plate. It can be seen from Figs. 9(b) and 9(c) that the small bubbles are close to the plate mostly in a vertical position. At the streamwise position far away from the injector as Figs. 9(d) and 9(e) show, bubble breakup is fully developed. Although most of the bubbles in the flow field are smaller than the initial volume, some large bubbles can still be seen obviously, which is the result of the coalescence of bubbles downstream. It should be noted that the maximum value of the color bar in Fig. 9 is set as  $200\text{ }\mu\text{m}$  for the purpose of better presentation. It does not mean that there are no bubbles with a diameter of more than  $200\text{ }\mu\text{m}$  in the flow field. In fact, a small number of bubbles can reach a diameter near  $250\text{ }\mu\text{m}$ , but these large bubbles are difficult to exist for a long time under turbulence.

More quantitative bubble distribution information is shown in Fig. 10, and the vertical distribution of bubble volume density at four typical downstream locations is plotted. At the same time, the boundary layer thickness and momentum thickness are also plotted to present a clear comparison. The x-coordinate  $\Delta x$  represents the streamwise distance from the injector. The most obvious conclusion drawn from the figure is that most of the bubble volume is concentrated in the near wall region. A large number of microbubbles are in the inner layer of the turbulent boundary layer, which is beneficial to drag reduction.<sup>13,24,29</sup> Because the bubble volume is very small due to the breakup, the vertical range that bubbles concentrate is smaller than the momentum thickness. However, the bubble concentration near the plate surface gradually weakens when moving downstream. Meanwhile, the range of bubble vertical migration movement becomes larger and larger downstream. Some bubbles move beyond the thickness of the turbulent boundary layer and reach the main flow region at

$\Delta x = 1$ . The change in bubble volume distribution changes the local viscosity and flow state, which will further affect the drag reduction effect.

Beneficial from the bubble breakup and coalescence simulation algorithms developed in the present study, the bubble size distribution can be predicted, compared, and analyzed. Figure 11 shows the comparison of bubble size distributions between numerical results and experimental data at two different streamwise positions. In general, the numerical prediction agrees well with the experimental data, especially at the downstream position  $\Delta x = 1\text{ m}$ . At the upstream measurement point, the numerical predicted average bubble diameter is about  $10\text{ }\mu\text{m}$  larger than the experimental results, and the predicted peak frequency is lower. This indicates that the bubble breakup is more violent in the experiment. The authors believe that the error is put down to the binary breakup hypothesis in the simulation algorithm. It is limited in the simulation that only two daughter bubbles are generated per breakup. However, actual bubble breakup in the experiment may be ternary or even multiple, which means that the development of bubble size distribution is faster than the present simulation. After the flow is fully developed downstream, the numerical results are in good agreement with the experimental measurement, which proves the effectiveness of the bubble breakup and coalescence modules in the present solver.

Five different vertical spatial ranges are selected for statistical analysis of bubble distribution in the wall-normal direction. Average bubble diameters in five ranges at two different streamwise positions are shown in Fig. 12. It is found that the closer to the upper plate, the smaller the average diameter of the bubble. This phenomenon is more obvious upstream, which is usually the effective region of drag reduction. The results indicate that the smaller bubbles are easier to enter the inner layer of the turbulent boundary layer. From the view of the fluid mechanism, larger bubbles will be subjected to greater fluid acceleration forces in turbulent boundary layers, which drive the bubbles more quickly toward the main flow. How to let more bubbles enter the inner layer of the turbulent boundary layer is one of the key problems

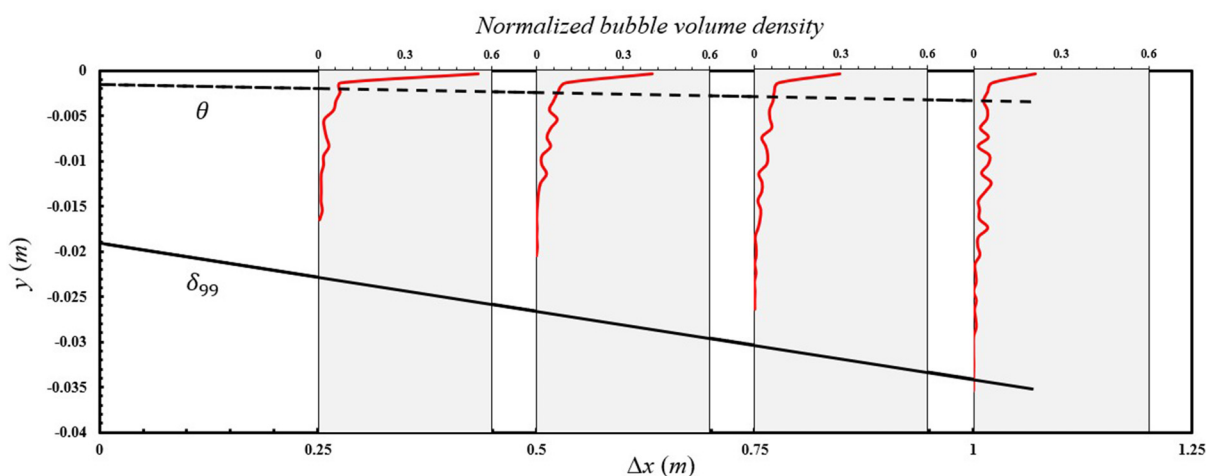
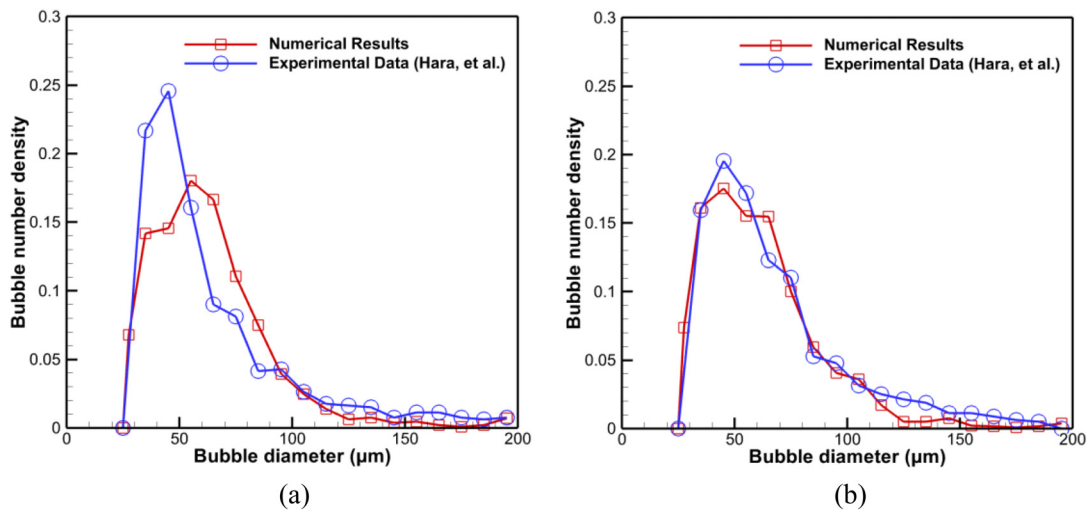
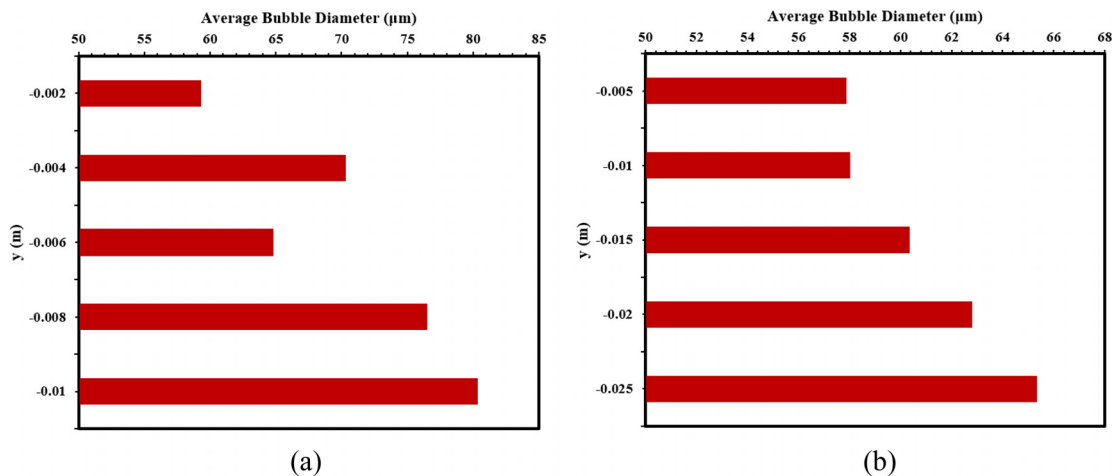


FIG. 10. Vertical distribution of bubble volume density at four typical downstream locations,  $\Delta x = 0.25$ ,  $\Delta x = 0.5$ ,  $\Delta x = 0.75$ , and  $\Delta x = 1$ . The air flow rate is  $Q = 30.25\text{ mm}^3/\text{s}$ . Turbulent boundary layer thickness (black solid line) and momentum thickness (black dashed line).



**FIG. 11.** Comparison of bubble size distributions between numerical results and experimental data at two different streamwise positions. The air flow rate is  $Q = 30.25 \text{ mm}^3/\text{s}$ . (a)  $\Delta x = 0.25$  and (b)  $\Delta x = 1$ .



**FIG. 12.** Wall-normal direction bubble size distribution at two different streamwise positions with air flow rate  $Q = 30.25 \text{ mm}^3/\text{s}$ . (a)  $\Delta x = 0.25$  and (b)  $\Delta x = 1$ .

of the bubble drag reduction technique. According to the present results, small microbubbles need to be produced in practical applications to improve the drag reduction effect.

### B. Drag reduction effect

Bubbles are injected into the turbulent flow field with three different air flow rates,  $Q = 30.25 \text{ mm}^3/\text{s}$ ,  $Q = 60.5 \text{ mm}^3/\text{s}$ , and  $Q = 90.75 \text{ mm}^3/\text{s}$ . The computational conditions are set according to the experiment of Hara *et al.*,<sup>15</sup> and the comparison of the drag reduction effect at two different streamwise positions is plotted in Fig. 13. Simulations both with and without bubble breakup and coalescence (b&c) algorithms are carried out.  $C_f$  and  $C_{f0}$  represent the frictional resistance coefficients with and without bubble injection, which are calculated using the local shear stress  $C_f = 2\tau_w/\rho U^2$ . The obvious

drag reduction effect can be obtained at the upstream position as shown in Fig. 13(a), especially with a higher air flow rate. This apparent trend is also reflected in both numerical simulations. However, the specific magnitudes are significantly different. With the increase in the air flow rate, the drag reduction effect at the upstream is improved from 9% to 20%. However, the drag reduction effect predicted by the simulation without b&c algorithms varies from 2% to 7%, which is much smaller than the experimental data. This indicates that the predicted bubble flow state in the turbulent boundary layer is different from that in the experiment. At the same time, the drag reduction effect predicted by the simulation with b&c algorithms varies from 5% to 12%, which is closer to the experimental data in contrast with the original one. The results indicate that considering bubble coalescence and breakup will increase the calculated drag reduction effect in the Euler-Lagrange method. For the results downstream as shown in



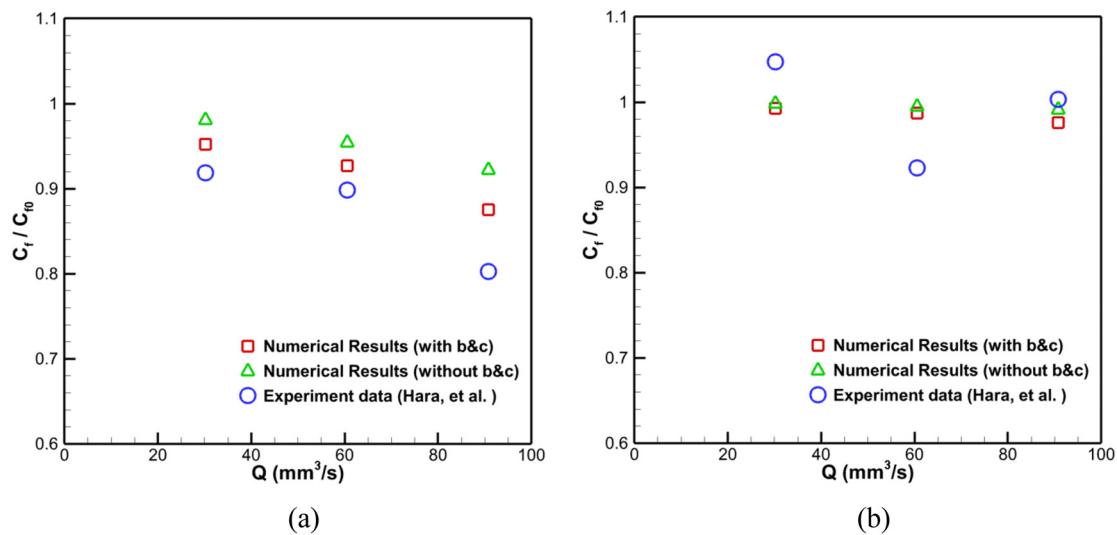


FIG. 13. Drag reduction effect at two different streamwise positions: (a)  $\Delta x = 0.25$  and (b)  $\Delta x = 1$ .

Fig. 13(b), the drag reduction effect is very limited. Numerical results are less than 2%, while the experimental results also fluctuate around the drag reduction effect of zero. By the analysis of bubble behavior characteristics in Sec. IV A, it is found that most of the downstream bubbles are away from the plate, resulting in the failure of drag reduction. In general, neither the new method with the b&c algorithm nor the original method without b&c has a certain difference from the experiment in the prediction of the drag reduction effect. The numerical results of the present work show that the new method will be helpful for the prediction at least in the upstream. Although it is not so obvious in values, it also indicates that bubble coalescence and breakup

have an influence on the flow evolution. The new method is more reasonable in physics.

Next, the drag reduction effect is further analyzed by means of visual figures. Figure 14 shows a transient bubble distribution at the position  $\Delta x = 0.25$  with and without b&c algorithms. The bubble flow rate is  $Q = 60.5 \text{ mm}^3/\text{s}$ . It can be found in Fig. 14(a) that bubbles with the initial diameter are more uniformly distributed in the turbulent boundary layer so that many bubbles cannot affect the flow in the near wall region. However, if breakup and coalescence are simulated, bubbles will not retain their initial sizes. A large amount of smaller bubbles stays in the near wall

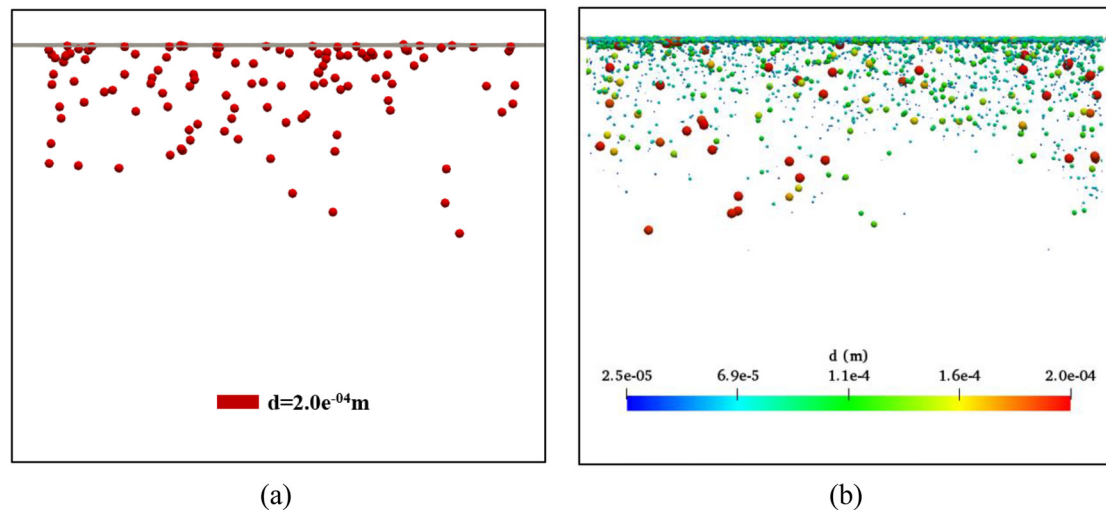
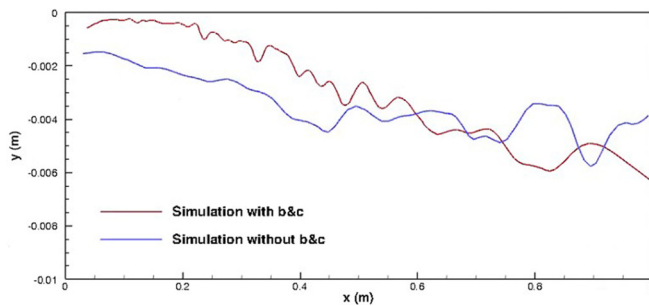


FIG. 14. Transient bubble distribution at the position  $\Delta x = 0.25$  for bubble flow rate  $Q = 60.5 \text{ mm}^3/\text{s}$ . (a) Simulation without b&c algorithms. (b) Simulation with b&c algorithms.



**FIG. 15.** Averaged bubble trajectory simulated by two different methods for the bubble flow rate  $Q = 60.5 \text{ mm}^3/\text{s}$ .

region as Fig. 14(b) shows. Microbubbles form a bubble layer on the surface of the plate, effectively reducing the local mixing viscosity of fluid. This is why the drag reduction effect predicted by the new simulation method with b&c is larger than that predicted by the original method and more consistent with the experimental data.

Figure 15 shows the comparison of averaged bubble trajectory between simulations with and without b&c algorithms. A significant difference can be observed upstream. With the action of the bubble breakup and coalescence algorithms, bubbles simulated by the new method are closer to the surface of the plate. When bubbles are injected into the flow field, breakup caused by the velocity difference and turbulent flow is the dominant bubble behavior. This phenomenon results in a significant difference between the results obtained by the two different methods. At the same time, the region close to the injector is the main effective region of the bubble drag reduction technique, which further emphasizes the necessity of simulating the bubble breakup and coalescence behavior. As the flow develops downstream, averaged bubble trajectories simulated by the two methods gradually

reach a similar state. Most bubbles migrate to the outer layer of the boundary layer and make little contribution to drag reduction.

### C. Turbulent flow modulation

Turbulent flow modulation due to bubble injection is a notable characteristic in the bubble drag reduction process. Statistical flow properties including the mean velocity profile and Reynolds stress are calculated and compared with and without bubbles. At the same time, simulation results with and without breakup and coalescence algorithms are also plotted.

Figure 16 shows the comparison of mean liquid velocity profiles under three different numerical conditions, including no bubble injection, BDR without the b&c algorithm, and BDR with the b&c algorithm. It can be seen that the bubbles mainly affect the viscous sublayer region and log-law region, which are also the main active regions of bubbles. The velocity of the bubbles near the wall is relatively low. These bubbles drag surrounding flow, leading to a decrease in flow velocity in the viscous sublayer. At the same time, bubbles gather near the wall, leading to a squeeze on the liquid flow away from the wall. As a consequence, there is an increase in fluid velocity in the log-law region. By comparing the results of the present numerical method with that of the original method, the effect of velocity profile modulation is more obvious. This is because more small bubbles obtained by the breakup and coalescence algorithm enter the viscous sublayer, which has a greater impact on the flow field.

Figure 17 shows the comparison of Reynolds stress profiles between single phase and two phase simulations. It can be seen that the main effect of bubbles is to reduce the peak value of Reynolds stress. The velocity fluctuation induced by bubble motion produces a Reynolds stress opposite to the original sign, leading to a significant decrease within the range  $10 < y^+ < 400$ . Specifically, in the simulation with bubble breakup and coalescence algorithms, the Reynolds stress decreases more obviously. According to the previous theoretical

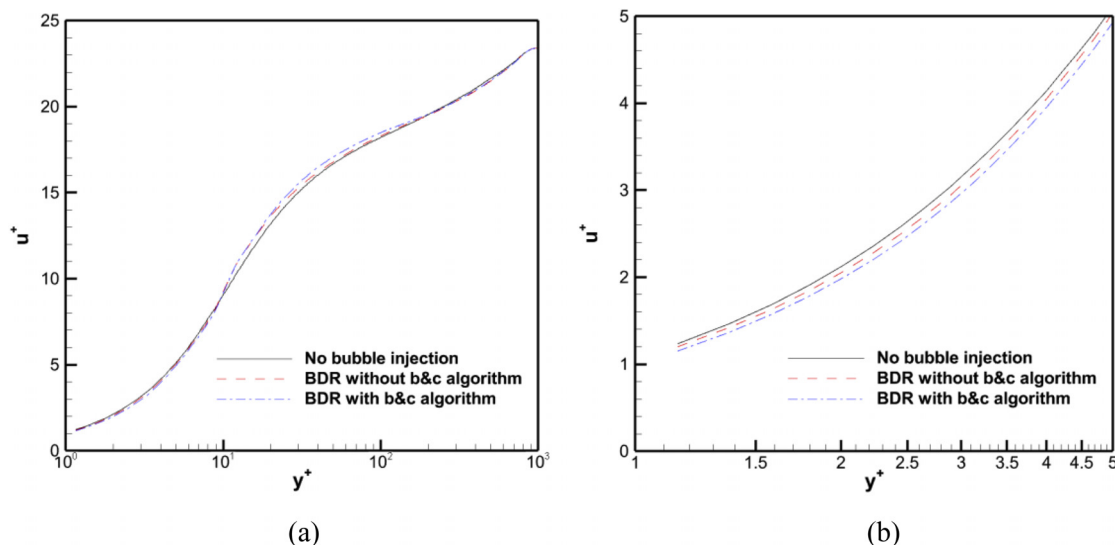


**FIG. 16.** Comparison of mean liquid velocity profiles between three different numerical conditions: (a) velocity profile inside the boundary layer and (b) local velocity profile inside the viscous sublayer.

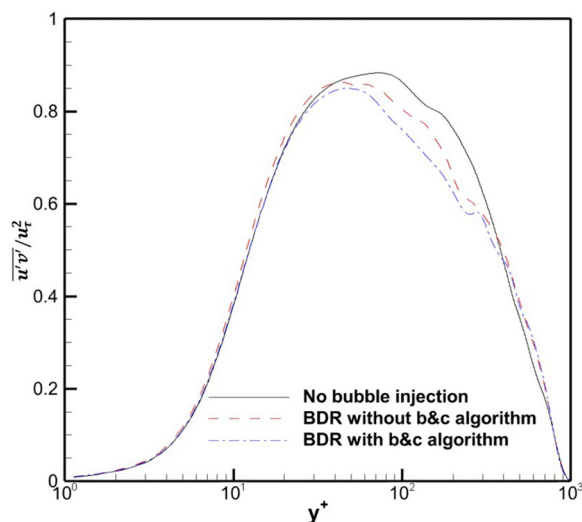


FIG. 17. Comparison of Reynolds stress profiles between three different numerical conditions.

analysis,<sup>8,11</sup> Reynolds stress is an important component of frictional drag in the turbulent boundary layer. Therefore, the reduction of the Reynolds stress peak value caused by bubbles is also beneficial to the reduction of frictional drag.

## V. CONCLUSIONS

In this paper, bubble drag reduction in turbulent boundary layer flow is simulated by the Euler–Lagrange method with the consideration of bubble breakup and coalescence. The main achievement is to be able to simulate the bubble size distribution, which is a breakthrough in the research on the bubble drag reduction problem of the Euler–Lagrange method. Detailed two phase flow analysis is carried out, and the following conclusions can be obtained:

- (1) Numerical algorithms of bubble breakup and coalescence for the Euler–Lagrange method are proposed and introduced in detail. These algorithms are successfully adopted to predict the bubble size distribution of the bubble drag reduction process in turbulent boundary layer flow. By comparison of flow characteristics, the drag reduction effect, and turbulent modulation, it has been proved that the simulation of bubble breakup and coalescence is necessary to obtain better results.
- (2) With the help of bubble breakup and coalescence simulation, bubble size statistical analysis is carried out. The results indicate that the smaller bubbles are easier to enter the inner layer of the turbulent boundary layer. Driving bubbles into the inner layer of the boundary layer is an important way to achieve an effective drag reduction. Therefore, small microbubbles need to be produced in practical applications to improve the drag reduction effect.
- (3) The influence of bubble size distribution is mainly reflected in the upstream region, which is also the main effective region of bubble drag reduction. When bubbles are injected into the flow field, breakup caused by the velocity difference and turbulent flow is the dominant bubble behavior. The bubble trajectory

obtained by the new numerical method is closer to the plate at the upstream and has a stronger influence on the flow state. As a result, the predicted drag reduction effect is also higher.

## ACKNOWLEDGMENTS

This work was supported by the National Natural Science Foundation of China (Grant Nos. 51909160 and 51879159) and the National Key Research and Development Program of China (Grant Nos. 2019YFB1704200 and 2019YFC0312400), for which the authors are most grateful.

## DATA AVAILABILITY

The data that support the findings of this study are available from the corresponding author upon reasonable request.

## REFERENCES

- <sup>1</sup>K. Fukuda, J. Tokunaga, T. Nobunaga, T. Nakatani, and T. Iwasaki, “Frictional drag reduction with air lubricant over a super-water-repellent surface,” *J. Mar. Sci. Technol.* **5**, 123–130 (2000).
- <sup>2</sup>Y. Gu, S. Yu, J. Mou *et al.*, “Experimental study of drag reduction characteristics related to the multifactor coupling of a bionic jet surface,” *J. Hydrodyn.* **31** (2), 186–194 (2019).
- <sup>3</sup>S. Wang, A. Zhang, Y. Liu *et al.*, “Bubble dynamics and its applications,” *J. Hydrodyn.* **30**(6), 975–991 (2018).
- <sup>4</sup>R. Latorre, A. Miller, and R. Philips, “Micro-bubble resistance reduction on a model SES catamaran,” *Ocean Eng.* **30**(17), 2297–2309 (2003).
- <sup>5</sup>P. Tuan and P. Huang, “Reduction ship skin resistance by injection small bubbles,” in *Oceans*, Hampton Roads, VA (2012).
- <sup>6</sup>I. Kumagai, Y. Takahashi, and Y. Murai, “Power-saving device for air bubble generation using a hydrofoil to reduce ship drag: Theory, experiments, and application to ships,” *Ocean Eng.* **95**, 183–194 (2015).
- <sup>7</sup>Y. Hassan, T. Gutierrez, and J. Jimenez-Bernal, “Temporal correlation modification by microbubbles injection in a channel flow,” *Int. Commun. Heat Mass Transfer* **32**, 1009–1015 (2005).
- <sup>8</sup>J. Ortiz-Villafuerte and Y. Hassan, “Investigation of microbubble boundary layer using particle tracking velocimetry,” *J. Fluids Eng.* **128**, 507–519 (2006).
- <sup>9</sup>Y. Murai, Y. Oishi, T. Sasaki, Y. Kodama, and F. Yamamoto, “Turbulent shear stress profiles in a horizontal bubbly channel flow,” in *Proceedings of 6th International Symposium on Smart Control of Turbulence*, Tokyo (2005), pp. 289–295.
- <sup>10</sup>Y. Murai, Y. Oishi, Y. Takeda *et al.*, “Turbulent shear stress profiles in a bubbly channel flow assessed by particle tracking velocimetry,” *Exp. Fluids* **41**(2), 343–352 (2006).
- <sup>11</sup>Y. Murai, H. Fukuda, Y. Oishi *et al.*, “Skin friction reduction by large air bubbles in a horizontal channel flow,” *Int. J. Multiphase Flow* **33**(2), 147–163 (2007).
- <sup>12</sup>S. Eric, S. L. Winkel, D. R. Ceccio, and M. P. Dowling, “Bubble-size distributions produced by wall injection of air into flowing freshwater, saltwater and surfactant solutions,” *Exp. Fluids* **37**, 802–810 (2004).
- <sup>13</sup>W. C. Sanders, E. S. Winkel, D. R. Dowling, M. Perlin, and S. L. Ceccio, “Bubble friction drag reduction in a high-Reynolds-number flat-plate turbulent boundary layer,” *J. Fluid Mech.* **552**, 353–380 (2006).
- <sup>14</sup>B. R. Elbing, E. S. Winkel, K. A. Lay, S. L. Ceccio, D. R. Dowling, and M. Perlin, “Bubble-induced skin-friction drag reduction and the abrupt transition to air-layer drag reduction,” *J. Fluid Mech.* **612**, 201–236 (2008).
- <sup>15</sup>K. Hara, T. Suzuki, and F. Yamamoto, “Image analysis applied to study on frictional-drag reduction by electrolytic microbubbles in a turbulent channel flow,” *Exp. Fluids* **50**, 715–727 (2011).
- <sup>16</sup>B. Paik, G. Yim, K. Y. Kim, and K. S. Kim, “The effects of microbubbles on skin friction in a turbulent boundary layer flow,” *Int. J. Multiphase Flow* **80**, 164–175 (2016).
- <sup>17</sup>R. F. Kunz, S. Deutsch, and J. W. Lindau, “Two fluid modeling of microbubble turbulent drag reduction,” in *Proceedings of FEDSM’03: 4th ASME-JSME Joint*

- Fluids Engineering Conference, Honolulu, Hawaii, Paper No. FED2003-45640 (2003).
- <sup>18</sup>R. F. Kunz, H. J. Gibeling, M. R. Maxey, G. Tryggvason, A. A. Fontaine, H. L. Petrie, and S. L. Ceccio, "Validation of two-fluid Eulerian CFD modelling for microbubble drag reduction across a wide range of Reynolds numbers," *J. Fluids Eng.* **129**, 66–79 (2007).
  - <sup>19</sup>X. Zhao, Z. Zong, Y. Jiang *et al.*, "Numerical simulation of micro-bubble drag reduction of an axisymmetric body using OpenFOAM," *J. Hydrodyn.* **31**(5), 900–910 (2019).
  - <sup>20</sup>K. Mohanaragam, S. C. P. Cheung, J. Y. Tu *et al.*, "Numerical simulation of micro-bubble drag reduction using population balance model," *Ocean Eng.* **36**(11), 863–872 (2009).
  - <sup>21</sup>S. Qin, N. Chu, Y. Yao *et al.*, "Stream-wise distribution of skin-friction drag reduction on a flat plate with bubble injection," *Phys. Fluids* **29**, 037103 (2017).
  - <sup>22</sup>J. Xu, M. R. Maxey, and G. E. Karniadakis, "Numerical simulation of turbulent drag reduction using micro-bubbles," *J. Fluid Mech.* **468**, 271–281 (2002).
  - <sup>23</sup>A. Ferrante and S. Elghobashi, "On the physical mechanisms of drag reduction in a spatially developing turbulent boundary layer laden with microbubbles," *J. Fluid Mech.* **503**, 345–355 (2004).
  - <sup>24</sup>M. Mattson and K. Mahesh, "Simulation of bubble migration in a turbulent boundary layer," *Phys. Fluids* **23**(4), 045107 (2011).
  - <sup>25</sup>M. Pang, J. Wei, B. Yu *et al.*, "Numerical investigation on turbulence and bubbles distribution in bubbly flow under normal gravity and microgravity conditions," *Microgravity Sci. Technol.* **22**(3), 283–294 (2010).
  - <sup>26</sup>D. Molin, C. Marchioli, and A. Soldati, "Turbulence modulation and micro-bubble dynamics in vertical channel flow," *Int. J. Multiphase Flow* **42**, 80–95 (2012).
  - <sup>27</sup>M. Pang, J. Wei, and B. Yu, "Numerical study on modulation of microbubbles on turbulence frictional drag in a horizontal channel," *Ocean Eng.* **81**, 58–68 (2014).
  - <sup>28</sup>K. S. Asiagbe, M. Fairweather, D. O. Njoubenwu, and M. Colombo, "Large eddy simulation of microbubble transport in a turbulent horizontal channel flow," *Int. J. Multiphase Flow* **94**, 80–93 (2017).
  - <sup>29</sup>X. Zhang, J. Wang, and D. Wan, "Euler–Lagrange study of bubble drag reduction in turbulent channel flow and boundary layer flow," *Phys. Fluids* **32**, 027101 (2020).
  - <sup>30</sup>F. Nicoud and F. Ducros, "Subgrid-scale stress modelling based on the square of the velocity gradient tensor flow," *Turbul. Combust.* **62**, 183–200 (1999).
  - <sup>31</sup>K. Guleren and A. Turan, "Validation of large-eddy simulation of strongly curved stationary and rotating U-duct flows," *Int. J. Heat Fluid Flow* **28**, 909–921 (2007).
  - <sup>32</sup>A. Tomiyama, G. P. Celata, S. Hosokawa, and S. Yoshida, "Terminal velocity of single bubbles in surface tension force dominant regime," *Int. J. Multiphase Flow* **28**, 1497–1519 (2002).
  - <sup>33</sup>A. Tomiyama, H. Tamai, I. Zun, and S. Hosokawa, "Transverse migration of single bubbles in simple shear flows," *Chem. Eng. Sci.* **57**, 1849–1858 (2002).
  - <sup>34</sup>S. Heitkam, A. E. Sommer, W. Drenckhan *et al.*, "A simple collision model for small bubbles," *J. Phys.: Condens. Matter* **29**(12), 124005 (2017).
  - <sup>35</sup>Y. Xiong, Q. Liang, S. Mahaffey *et al.*, "A novel two-way method for dynamically coupling a hydrodynamic model with a discrete element model (DEM)," *J. Hydrodyn.* **30**(5), 966–969 (2018).
  - <sup>36</sup>Y. Lau, W. Bai, N. Deen, and J. Kuipers, "Numerical study of bubble break-up in bubbly flows using a deterministic Euler–Lagrange framework," *Chem. Eng. Sci.* **108**, 9–22 (2014).
  - <sup>37</sup>M. Prince and H. Blanch, "Bubble coalescence and break-up in air-sparged bubble columns," *AIChE J.* **36**, 1485–1499 (1990).
  - <sup>38</sup>F. Risso and J. Fabre, "Oscillations and breakup of a bubble immersed in a turbulent field," *J. Fluid Mech.* **372**, 323–355 (1998).
  - <sup>39</sup>N. I. Kolev, *Multiphase Flow Dynamics 1: Fundamentals*, 3rd ed. (Springer, Berlin, 2007).
  - <sup>40</sup>H. Luo and H. F. Svendsen, "Theoretical model for drop and bubble breakup in turbulent dispersions," *AIChE J.* **42**(5), 1225–1233 (1996).
  - <sup>41</sup>C. Martínez-Bazán, J. L. Montañés, and J. C. Lasheras, "On the breakup of an air bubble injected into fully developed turbulent flow. Part 1. Breakup frequency," *J. Fluid Mech.* **401**, 157–182 (1999).
  - <sup>42</sup>G. Narsimhan and J. P. Gupta, "A model for transitional breakage probability of droplets in agitated lean liquid–liquid dispersions," *Chem. Eng. Sci.* **34**, 257–265 (1979).
  - <sup>43</sup>F. Lehr, M. Millies, and D. Mewes, "Bubble size distributions and flow fields in bubble columns," *AIChE J.* **48**(11), 2426–2443 (2002).
  - <sup>44</sup>D. K. R. Nambiar, R. Kumar, T. R. Das, and K. S. Gandhi, "A new model for the breakage frequency of drops in turbulent stirred dispersions," *Chem. Eng. Sci.* **47**(12), 2989–3002 (1992).
  - <sup>45</sup>X. Zhang, J. Wang, and D. Wan, "Numerical simulation of bubble breakup and coalescence in a turbulent boundary layer flow," in *Proceedings of the Thirtieth International Ocean and Polar Engineering Conference*, Shanghai, China, October 11–16, 2020.
  - <sup>46</sup>J. Xue, F. Chen, N. Yang *et al.*, "Eulerian–Lagrangian simulation of bubble coalescence in bubbly flow using the spring-dashpot model," *Chin. J. Chem. Eng.* **25**, 249–256 (2017).
  - <sup>47</sup>R. Kirkpatrick and M. Lockett, "Influence of approach velocity on bubble coalescence," *Chem. Eng. Sci.* **29**, 2363–2373 (1974).
  - <sup>48</sup>T. Mukha and M. Liefvendahl, "The generation of turbulent inflow boundary conditions using precursor channel flow simulations," *Comput. Fluids* **156**, 21–33 (2017).
  - <sup>49</sup>T. Mukha and M. Liefvendahl, "Eddylicious: A python package for turbulent inflow generation," *SoftwareX* **7**, 112–114 (2018).
  - <sup>50</sup>N. J. Georgiadis, D. P. Rizzetta, and C. Fureby, "Large-eddy simulation: Current capabilities, recommended practices, and future research," *AIAA J.* **48**, 1772–1784 (2010).
  - <sup>51</sup>J. Kim, P. Moin, and R. D. Moser, "Turbulence statistics in fully developed channel flow at low Reynolds number," *J. Fluid Mech.* **177**, 133–166 (1987).
  - <sup>52</sup>P. Schlatter and R. Örlü, "Assessment of direct numerical simulation data of turbulent boundary layers," *J. Fluid Mech.* **659**, 116–126 (2010).
  - <sup>53</sup>A. J. Smits, N. Matheson, and P. N. Joubert, "Low-Reynolds-number turbulent boundary layers in zero and favorable pressure gradients," *J. Ship Res.* **27**, 147–157 (1983).